




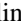




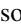





Dissociative electron recombination and rotational cooling of the deuterated triatomic hydrogen ions H_2D^+ and D_2H^+

A. Znotins ¹, A. Faure,² C. H. Greene ³, M. Grieser ¹, F. Grussie,¹ L. W. Isberner ^{1,4}, Á. Kálosi ^{1,5}, V. Kokoouline ⁶, D. Müll ¹, D. Paul ¹, M. Pezzella,^{7,8} D. W. Savin ⁵, S. Schippers ⁴, J. Tennyson ⁷, A. Wolf ¹, O. Novotný ¹ and H. Kreckel ^{1,*}

¹Max-Planck-Institut für Kernphysik, Saupfercheckweg 1, 69117 Heidelberg, Germany

²Université Grenoble Alpes, CNRS, IPAG, 38000 Grenoble, France

³Department of Physics and Astronomy, Purdue University, West Lafayette, Indiana 47907, USA

⁴I. Physikalisches Institut, Justus-Liebig-Universität Gießen, 35392 Gießen, Germany

⁵Columbia Astrophysics Laboratory, Columbia University, New York, New York 10027, USA

⁶Department of Physics, University of Central Florida, Orlando, Florida 32816, USA

⁷Department of Physics and Astronomy, University College London, London WC1E 6BT, United Kingdom

⁸Dipartimento di Farmacia, Università 'G. d'Annunzio Chieti-Pescara, via dei Vestini, 66100 Chieti, Italy



(Received 19 September 2025; accepted 20 October 2025; published 17 November 2025)

We have measured the dissociative recombination (DR) of the deuterated triatomic hydrogen ions H_2D^+ and D_2H^+ as a function of storage time at the Cryogenic Storage Ring (CSR). Both molecular ions were stored for up to 1000 s inside the cryogenic vacuum of the CSR prior to the electron recombination measurements, allowing them to cool to their lowest rotational states. We implement a comprehensive model for all relevant processes to predict the internal state evolution of the ions during storage inside the CSR, employing calculated radiative transition strengths and state-selective rate coefficients for electron collisions. Our DR rate coefficient measurements with deuterated triatomic hydrogen ions in defined quantum states allow for meaningful comparisons with state-of-the-art theoretical calculations, paving the way for a better understanding of the complex DR process for polyatomic molecular ions.

DOI: [10.1103/wfb2-9lfw](https://doi.org/10.1103/wfb2-9lfw)

I. INTRODUCTION

More than 300 different molecular species have been identified in the space between the stars [1], despite the fact that the physical conditions in the interstellar medium (ISM) do not appear favorable for chemical reactions. The key to the gas-phase chemistry in the cold ISM is the presence of molecular ions, as ion-neutral reactions typically proceed efficiently even at low temperature and density [2,3]. In this framework, the triatomic hydrogen ion H_3^+ is one of the most important species, initiating the formation of larger molecules through a series of proton-hop reactions [4,5]. In interstellar clouds, these chemical reactions compete with the dissociative recombination (DR) process, where the H_3^+ ions capture a free electron and break up into neutral atomic (H) and/or molecular (H_2) fragments. The DR of H_3^+ has a particularly large impact on the chemistry of the diffuse ISM [6], where it constitutes the dominant destruction process for H_3^+ [7].

The history of DR measurements with H_3^+ is somewhat turbulent, as measurements conducted with various techniques resulted in absolute rate coefficients that differed by orders of magnitudes at times [8–10]. However, storage ring measurements employing cold ion sources at different facilities [7,11–15] combined with state-of-the-art theoretical calculations [16–19] have largely settled the discussion on the overall scale of the H_3^+ DR rate coefficient. Nevertheless, some lingering doubts about the individual states populated in the storage ring experiments remain [13,14], and truly state-selective DR measurements have only recently become experimentally feasible for molecules with a permanent dipole moment [20–23].

Further experimental efforts toward state-selective DR measurements with H_3^+ are underway [24]. Nevertheless, already the current consensus [7,12] has enhanced our understanding of the chemistry of the ISM considerably. Observations of H_3^+ have been used to infer the cosmic-ray ionization rate in diffuse lines of sight [25,26] and shed light on physical conditions in the galactic center [27–29].

The deuterated isotopologs H_2D^+ and D_2H^+ can be detected in the denser regions of interstellar clouds. In conjunction with chemical models, observations of H_2D^+ have been used to infer the lifetime of the dense cores in star forming regions [30]. However, a recent study found unexpected D_2H^+ -to- H_2D^+ abundance ratios in a pre-stellar core, emphasizing the need to understand all relevant inelastic and

*Contact author: holger.kreckel@mpi-hd.mpg.de

Published by the American Physical Society under the terms of the Creative Commons Attribution 4.0 International license. Further distribution of this work must maintain attribution to the author(s) and the published article's title, journal citation, and DOI. Open access publication funded by Max Planck Society.

reactive rate coefficients for triatomic hydrogen and its deuterated isotopologs [31].

It should be noted that the H_3^+ DR rate coefficient cannot simply be applied to the deuterated species. Since the low-energy DR of triatomic hydrogen proceeds through the so-called *indirect process*, where the electron is initially captured into a Rydberg state of the neutral, the exact positions of excited state resonances play a crucial role, and they vary considerably for different isotopologs. Consequently, theoretical calculations predict marked differences for the low-temperature DR rate coefficients of H_2D^+ and D_2H^+ [32].

Here we report DR measurements for H_2D^+ and D_2H^+ ions as a function of storage time inside the extreme vacuum of the Cryogenic Storage Ring (CSR) [33]. Our work expands on our recent DR measurements with rotationally cold D_2H^+ ions [23] by studying the time dependence of the DR rate coefficient for both ion species in detail. Moreover, we present comprehensive models of the internal cooling, employing updated theoretical rate coefficients for inelastic and dissociative electron collisions, for both ions.

II. EXPERIMENT

We employed the CSR at the Max Planck Institute for Nuclear Physics in Heidelberg, Germany, for our measurements. The CSR is a fully cryogenic storage ring with 35 m circumference. Housed inside a big cryostat, the inner vacuum chambers can be cooled to ~ 6 K by a closed-loop liquid helium refrigeration system. The electrostatic ion optical lattice allows for storage of positive or negative ions with kinetic energies of up to 300 keV per unit charge. An array of ion sources and two independent electrostatic acceleration platforms are used to supply atomic or molecular ion beams to the storage ring. Technical details of the CSR facility and its infrastructure can be found in a previous publication [33].

A low-energy electron cooler in one of the straight sections of the storage ring provides a nearly monoenergetic electron beam that is superimposed collinearly to the stored ions. At matched velocities, Coulomb interactions between the electrons and the stored ions lead to phase-space cooling of the ion beam [34]. By detuning the electron beam velocity, the relative energy for electron-ion encounters in the center-of-mass frame can be adjusted very precisely, allowing for energy-resolved studies of electron-ion collisions.

A. Ion beam preparation

We measured the electron recombination of H_2D^+ and D_2H^+ separately. Both ions were produced in a duoplasmatron ion source and accelerated to 250 keV by an electrostatic high voltage platform. Coarse mass selection was achieved by a dipole magnet. This simple mass-selection stage is sufficient to prepare a pure D_2H^+ beam, because there are no molecular isobars in the beam with a mass of 5 u. The situation is more complicated for H_2D^+ , as D_2^+ ions are known to constitute a significant contaminant for H_2D^+ ion beams. To assess and minimize the fraction of D_2^+ in the ion beam, we utilized the isochronous mass spectrometry technique inside the CSR [35]. In this mode of operation, the initial momentum spread

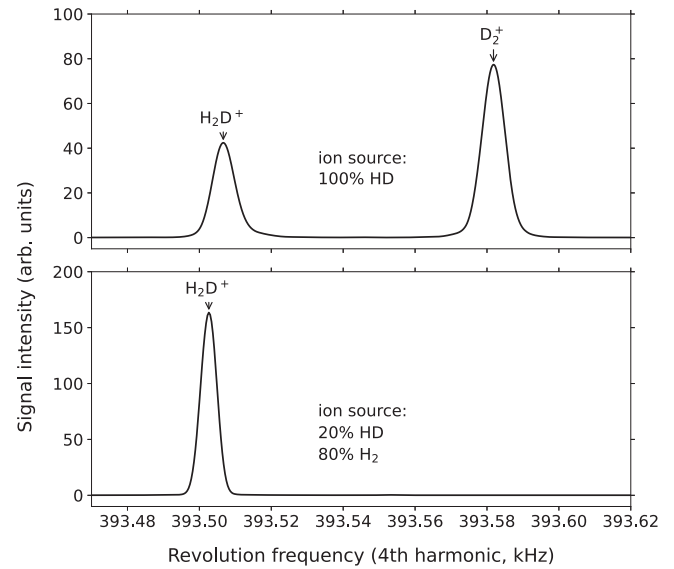


FIG. 1. Frequency spectrum (fourth harmonic) of the stored ions recorded with an electronic pickup electrode. Upper panel: Initial low pressure ion source settings using HD gas. The two peaks represent two different ion species, namely H_2D^+ and D_2^+ , which are stored simultaneously inside the CSR. Lower panel: Optimized ion source settings to suppress the D_2^+ contaminant, using a gas mixture of 20% HD and 80% H_2 and higher pressure inside the source. The D_2^+ peak is now undetectable, with an upper limit of 0.03% for the relative signal strength.

of the ion beam is compensated by the ion-optical lattice of the storage ring, and even small contaminations of molecular isobars can be detected through the analysis of the revolution frequency of the stored ions detected by pickup electrodes inside the ring.

The revolution frequency f of H_2D^+ ions at a kinetic energy of 250 keV inside the CSR is ~ 98.4 kHz. Figure 1 shows the fourth harmonic of the revolution frequency (where we define the integer multiple $n \times f$ as the n th harmonic). For low pressure settings of the duoplasmatron ion source, using HD gas (upper panel), the diatomic component in the form of D_2^+ is stronger than the H_2D^+ component. For optimized ion source settings, using a 4:1 H_2/HD gas mixture (lower panel) and overall higher pressure to favor the formation of triatomic ions inside the ion source, we were able to suppress the D_2^+ contaminant and get an essentially pure H_2D^+ ion beam. Note that the changing plasma potential for different ion source settings leads to a slight difference in the energy of the ion beam, which translates into a small shift of the H_2D^+ peak position. For these ion source settings the D_2^+ component was no longer detectable, and we inferred an upper limit for the fractional D_2^+ contamination of 3×10^{-4} .

B. Electron recombination measurements

The CSR low energy electron cooler occupies one of the straight sections of the storage ring. For the present experiments it is used to improve the ion beam quality through phase-space cooling [34] and at the same time as an electron target for the recombination measurements. Electron cooling requires an electron beam that is velocity matched and

superimposed collinearly on the stored ions. The CSR is currently the only electrostatic storage facility in the world that reaches high-enough ion beam energies for electron cooling. For singly charged ion beams at kinetic energies from 40 to 300 keV, typical electron beam energies for merged-beams experiments range from 1–50 eV. Here the technical challenge lies in the low-energy limit, specifically in providing well-defined electron beams with energies as low as 1 eV in the laboratory frame, while maintaining an internal energy spread in the range 1–2 meV.

In the CSR cooler the electrons are released from a gallium arsenide photocathode by a 808-nm laser. The electrons are produced inside a strong magnetic field that is gradually relaxed upon extraction to expand the electron beam adiabatically and thus reduce the transverse temperature [36]. The electrons are typically transported toward the CSR at a kinetic energy on the order of 50 eV, before they are accelerated or decelerated to their final energy by drift tubes inside the CSR overlap region. For 250 keV H_2D^+ and D_2H^+ ions, velocity-matching conditions are achieved by electron beams at ~ 34 and ~ 27 eV in the laboratory frame, respectively. Typical densities for electron cooling in the present experiments were on the order of 10^5 cm^{-3} , but the electron beam duty cycle was reduced during long cooling phases, as the electron recombination process can limit the ion beam lifetime.

For energy-resolved electron-ion collision experiments the electron beam energy is detuned from the nominal cooling energy at matched velocities. We define the merged-beams detuning energy

$$E_d = (\sqrt{E_e} - \sqrt{E_0})^2, \quad (1)$$

as the center-of-mass collision energy for an electron beam at energy E_e with respect to the laboratory frame energy of the electron beam E_0 at matched ion-electron velocities, implicitly approximating the reduced mass of the collision system by the electron mass.

A large detector based on microchannel plates downstream of the electron cooler collects the neutral products resulting from recombination events. To infer the count rate for DR events only, the total count rate is corrected for non-electron-induced events by subtracting the background rate recorded while the electron beam is switched off. Combined with the electron density and the number of ions stored in the ring, which are measured routinely at the CSR, the count rate yields the absolute merged-beams rate coefficient α^{mb} . The total systematic uncertainty is assumed to be 20%, with the main contributions arising from the ion current determination (12.5%) and the uncertainty in the electron density (10%). To compare the experimental α^{mb} with theory, we average the product of theoretical cross sections σ and the relative velocity v_r , using the known electron-ion velocity distribution in the electron cooler for each detuning energy E_d

$$\alpha^{\text{mb}}(E_d) = \langle \sigma v_r \rangle. \quad (2)$$

For more details on the determination of experimental merged-beams rate coefficients α^{mb} and on the convolution procedure, see our previous work [21,22,37].

III. THEORY

The theoretical treatment of the DR for polyatomic ions remains a challenging task, and the case of triatomic hydrogen has received much attention. Owing to the lack of dissociative neutral states crossing the ionic potential at low energies, initial considerations concluded that the DR of H_3^+ should be extremely slow [38]. Early calculations of the direct DR process agreed roughly with the rate coefficient at high energies [39]; however, calculations of the low-energy-rate coefficient were orders of magnitude below the experimental values [40]. The situation improved significantly when the Jahn-Teller symmetry-distortion effect was identified as the key mechanism for the DR of H_3^+ at low energies [16], as subsequent calculations agreed well with the absolute scale of the experimental rate coefficient [17–19].

The H_3^+ ion has the shape of an equilateral triangle in its ground state, and its rotational level structure is that of a symmetric top. This symmetry is lifted in the deuterated variants, making them both asymmetric top molecules, belonging to the C_{2v} point group. The three vibrational modes are denoted ν_1 , ν_2 , ν_3 , while the rotational angular momentum is denoted J , and the two projection quantum numbers are K_a and K_c (for details on nomenclature and definition of quantum numbers see Ref. [41] and references therein).

Both molecular ions exist in two different nuclear spin modifications, named *ortho* and *para*. The nuclear spin symmetries are determined by the behavior of the wave function under permutation of identical particles. Therefore, the H_2D^+ case closely follows the classification of the H_2 molecule, while the D_2H^+ case resembles the scheme for the D_2 molecule. Through the symmetry requirements of the total wave function, the nuclear spin configuration imposes restrictions on the rotational quantum numbers of the molecules. Table 1 lists the symmetries, multiplicities, and the corresponding rotational quantum numbers for both molecular ions. Figure 2 shows the energy level scheme for the lowest rotational states (with $J \leq 2$) for both ions, together with the calculated radiative lifetimes [41] (spontaneous emission only) of the individual states. Since radiative transitions do not change the nuclear spin, the *ortho* and *para* states are depicted separately.

The theoretical framework for the adaptation of the DR calculations to the reduced symmetry of the deuterated species has been described in detail in Ref. [42]. We have updated those calculations with some changes to the way the channel functions for electron-ion scattering are constructed. These changes are documented in detail for the D_2H^+ ion in the supplemental material in Ref. [23].

While in the present study, we have used essentially the same model for the $e^- \text{-H}_3^+$ reactance matrix—in terms of dependence on the internuclear distances of the target ion—as in Refs. [18,43], the parameters of the model were obtained directly from the electron-scattering $e^- \text{-H}_3^+$ calculations. This is in contrast to the previous studies [18,43], which used the parameters derived from bound-state calculations by Mistrík *et al.* [44]. The updated parameters of the model (Eqs. (18) and (19) of Ref. [43]) are the following: $\mu_{\pm}^0 = 0.37$, $\delta = -4100 \text{ cm}^{-1}$, and $\lambda = -32000 \text{ cm}^{-1}$, compared to the

TABLE I. Nuclear spin configurations and symmetry restrictions for the rotational projection quantum numbers K_a and K_c of the H_2D^+ and D_2H^+ ions. The nuclear spins I_{H_2} (I_{D_2}) of the proton (deuteron) pairs and those of the deuteron (I_{D}) and the proton (I_{H}), respectively, are considered separately here, as we expect hyperfine interactions to be negligible. The numbers in parentheses denote the multiplicities.

H_2D^+		
Configuration (weight)	Ortho (9)	Para (3)
H_2 : Symmetry	A_1	B_2
Nuclear spin (weight)	$I_{\text{H}_2} = 1$ (3)	$I_{\text{H}_2} = 0$ (1)
D : Symmetry	A_1	A_1
Nuclear Spin (weight)	$I_{\text{D}} = 1$ (3)	$I_{\text{D}} = 1$ (3)
Rotational quantum numbers	K_a odd	K_a even
D_2H^+		
Configuration (weight)	Ortho (12)	Para (6)
D_2 : Symmetry	A_1	B_2
Nuclear spin (weight)	$I_{\text{D}_2} = 0$ (1)	$I_{\text{D}_2} = 1$ (3)
H : Symmetry	A_1	A_1
Nuclear Spin (weight)	$I_{\text{H}} = \frac{1}{2}$ (2)	$I_{\text{H}} = \frac{1}{2}$ (2)
Rotational quantum numbers	$K_a + K_c$ even	$K_a + K_c$ odd

values $\mu_{\pm}^0 = 0.395$, $\delta = -3424 \text{ cm}^{-1}$, and $\lambda = -38830 \text{ cm}^{-1}$ that were used in Refs. [18,43].

Figures 3 and 4 show the calculated rate coefficients for the DR of H_2D^+ and D_2H^+ , respectively. For the comparison to the storage ring results, we have convolved the calculated DR cross sections with the known electron velocity distribution inside the CSR electron cooler to yield the equivalent of merged-beams rate coefficients.

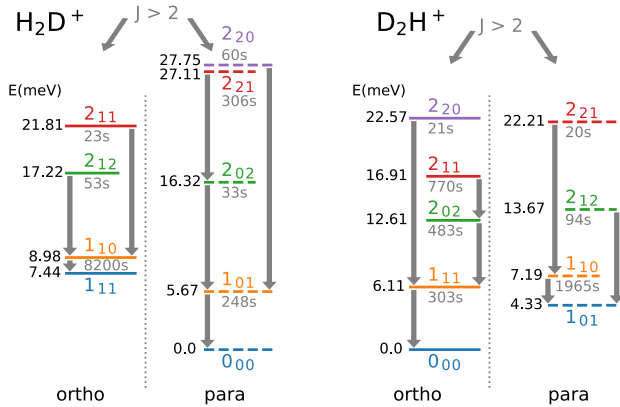


FIG. 2. Energy level schemes and radiative cooling transitions for H_2D^+ and D_2H^+ depicting all states with $J \leq 2$. The states are sorted into the respective ortho and para manifolds, as radiative transitions cannot change the nuclear spin. The labels in color denote the rotational quantum numbers $J_{K_a K_c}$. The radiative lifetimes of the excited states are given in gray at each level. The individual energies are given to the left of each level (in milli-electronvolts). The dark gray arrows indicate the dominant radiative decay transitions. The color code applied for the levels within each manifold (in energetically ascending order: blue, orange, green, red, purple) will be used throughout the manuscript.

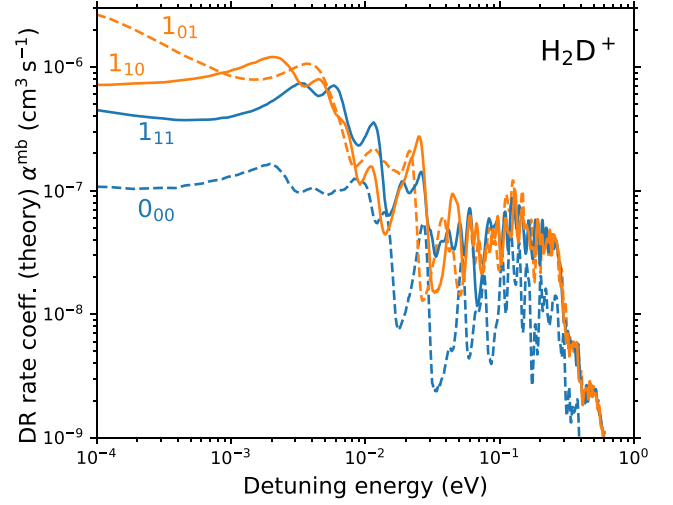
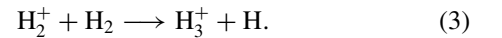


FIG. 3. Theoretical merged-beams DR rate coefficients for the four lowest rotational states of H_2D^+ . The rate coefficients were derived from DR cross-section calculations that were convolved with the known electron-velocity distribution of the CSR electron cooler. Ortho states are depicted by solid lines and para states by dashed lines.

The calculations show pronounced differences in the low-energy structures for the lowest rotational states of both ions. As H_2D^+ has fewer states that will be present in the CSR at very long storage times than D_2H^+ , we restrict our analysis to the four lowest rotational states ($J \leq 1$), while we consider all states with $J \leq 2$ for D_2H^+ .

IV. INTERNAL STATE EVOLUTION DURING STORAGE

The formation of triatomic hydrogen ions from H_2 gas in standard discharge ion sources proceeds through the electron impact ionization of H_2 , followed by the ion-neutral reaction



This reaction is very efficient and highly exothermic, releasing 1.76 eV of energy that will to a large extent end up as internal excitation of the H_3^+ ions [45]. The exothermicity of the formation reaction changes only by some milli-electronvolts for the formation of the deuterated variants [45]. Consequently, triatomic hydrogen ions produced in discharge ion sources usually feature internal energies that correspond to thousands of kelvin in temperature [46,47] (although the excitation does not necessarily have to follow a thermal distribution).

As radiative transitions do not change the nuclear spin of H_2D^+ or D_2H^+ molecules, cooling by photon emission will proceed strictly within the respective ortho or para manifolds. In contrast to H_3^+ , both deuterated triatomic hydrogen ions feature permanent dipole moments of 0.6 D for H_2D^+ [48] and 0.49 D for D_2H^+ [49]. As a consequence, H_2D^+ and D_2H^+ cool much more efficiently through spontaneous emission of radiation than H_3^+ . Furthermore, H_2D^+ and D_2H^+ do not possess extremely long-lived metastable rotational states, which pose a major challenge for storage ring measurements with H_3^+ [50].

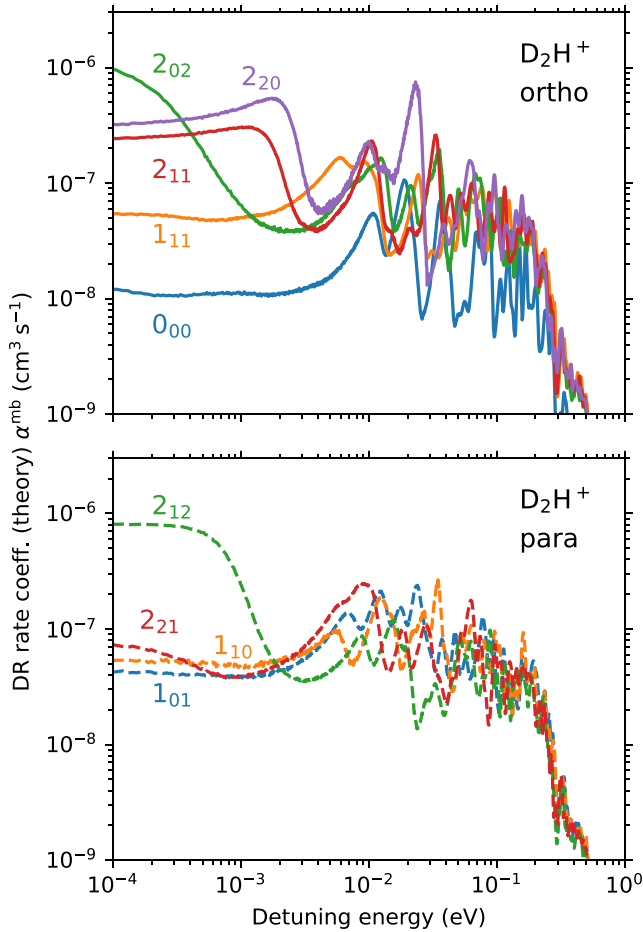


FIG. 4. Theoretical merged-beams DR rate coefficients for all rotational states of D_2H^+ with $J \leq 2$. The rate coefficients were derived from DR cross-section calculations that were convolved with the known electron-velocity distribution of the CSR electron cooler. For clarity, ortho and para states are plotted in different panels. Ortho states are depicted by solid lines (upper panel) and para states by dashed lines (lower panel).

A. Radiative cooling

We created a comprehensive master equation model of the internal cooling for both ions as a function of storage time inside the CSR. The model has been described previously in the Methods section of Ref. [23] for the D_2H^+ molecular ion. In brief, we simulate the time evolution of the population of all rovibrational states of H_2D^+ and D_2H^+ by a large set of ordinary coupled differential equations. The state energies for both ions and all radiative transitions are adapted from the most recent ExoMol linelist [41]. The H_2D^+ model encompasses 33 thousand states and 22 million transitions, while the D_2H^+ model consists of 50 thousand states and 41 million transitions. Both sets of states are more than sufficient to accurately cover a 3000 K Boltzmann distribution, which we use as a rough estimate of the average internal energy of the molecular ions extracted from a discharge ion source [46]. As in previous cooling studies, we neglect stimulated emission. While spontaneous decay dominates the cooling, we will also explore the influence of the blackbody radiation field inside

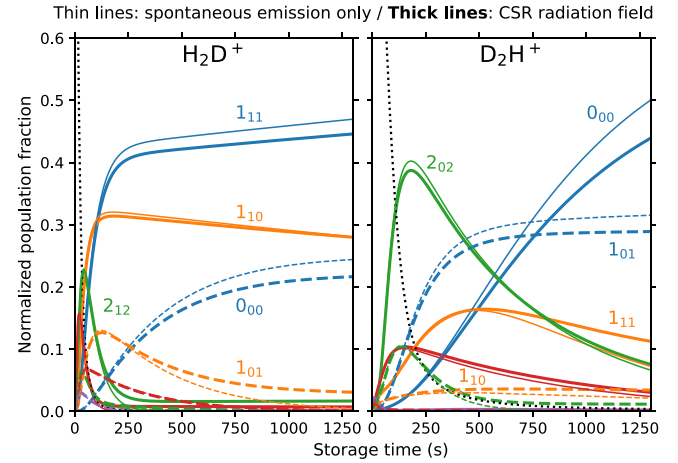


FIG. 5. Calculated evolution of the relative populations of all rotational states with $J \leq 2$ of H_2D^+ (left-hand side) and D_2H^+ (right-hand side) during storage for 1300 s inside the CSR. The thick lines depict the populations under the influence of the CSR radiation field, while the thin lines represent the evolution neglecting blackbody radiation. Ortho states are shown by solid lines; para states are shown by dashed lines. The color code for the individual levels is adapted from Fig. 2. Five of the most relevant rotational states for the long-term evolution are labeled explicitly. The dotted black lines show the evolution of the sum of the populations in states with $J > 2$.

the CSR and state-changing electron collisions in the next sections.

As it is our goal to prepare molecular ensembles in defined quantum states, it is informative to consider the energies and lifetimes of the lowest rotational states. The rotational levels and dominant radiative transitions among states with $J \leq 2$ are shown in Fig. 2 for both ions. In general, the lifetimes of states with $J > 2$ decrease with increasing energy, as more decay channels become available. Considering the lifetimes of the lowest rotational states, it becomes apparent that storage times of several hundred seconds are required to confine the populations of both ions to a handful of identifiable states. Additional cooling can be achieved through inelastic electron collisions, as we will show below.

Figure 5 depicts the time-dependent populations of the lowest rotational states of H_2D^+ and D_2H^+ , respectively. The thin lines represent the rotational state evolution in a radiation-free environment, where the spectral energy density is artificially set to zero. We simulate cooling by starting from a 3000 K Boltzmann distribution, where the population is dispersed over hundreds of individual states. We verified that the initial ion temperature has almost no impact on the final populations (as long as the temperature exceeds 1000 K), since all highly excited states decay very quickly.

In Fig. 5, the initial calculations (thin lines) neglect the radiation field inside the CSR, while the thick lines show the influence of the blackbody radiation field inside the storage ring. We adopt a standard CSR radiation field as inferred from previous studies [51], where we assume that 99% of the surface area is at the nominal chamber temperature of 6 K and 1% of the surfaces represent leaks from room temperature radiation (laser viewports and beamline ports). The calculations show that the presence of the radiation field changes

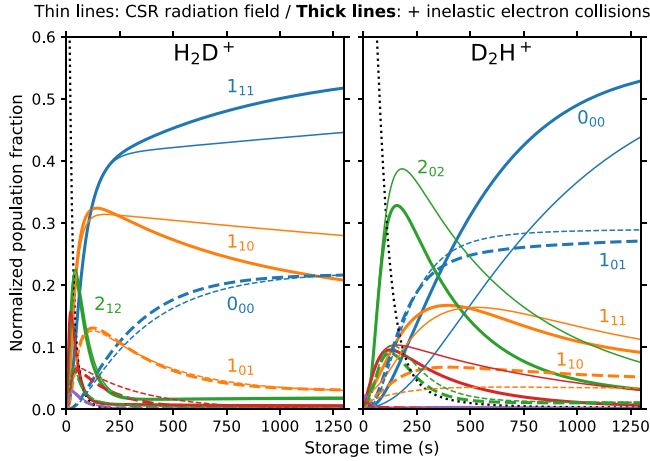


FIG. 6. Calculated evolution of the relative populations of rotational states of H_2D^+ and D_2H^+ during storage. The thick lines depict the populations when both the influence of the CSR radiation field as well as inelastic electron collisions are taken into account, while the thin lines represent the evolution without electron collisions. Ortho states are shown by solid lines, para states are shown by dashed lines. The color code for the individual levels is adapted from Fig. 2. The dotted black lines show the evolution of the sum of the populations in states with $J > 2$.

individual relative populations by up to $\sim 6\%$. Moreover, after 1300 s of storage, radiative cooling is still ongoing, and full equilibrium with the radiation field has not been reached.

B. Inelastic electron collisions

State-changing inelastic electron collisions are included through the relevant $J_\tau \rightarrow J'_\tau$ transitions among the lowest rotational states. The cross sections of electron impact excitation $\sigma_{J_\tau \rightarrow J'_\tau}(E)$ as a function of collision energy E were obtained from dedicated calculations, performed by combining R-matrix calculations with the fixed-nuclei (FN) and Coulomb-Born (CB) approximations, which were convolved with our experimental electron velocity distribution. Details on the cross-section calculations can be found in the supplemental material of Ref. [23]. The corresponding de-excitation cross sections $\sigma_{J'_\tau \rightarrow J_\tau}(E)$ were calculated using detailed balance. Figure 6 shows the effect of the inelastic electron collisions on the populations of the energetically lowest rotational states for the measurement conditions of the CSR experiments.

We considered state-changing collisions for H_2D^+ and D_2H^+ that involve any of the states with $J \leq 2$ as the energetically lower state of the transition. For the entire simulation we used a constant electron density of $0.55 \times 10^5 \text{ cm}^{-3}$, which represents the effective electron density during the cooling phase, before the measurement procedure starts. Throughout the measurement phase, the electron energy was detuned and scanned for short periods of time (see also beginning of Sec. V). While this procedure may induce small changes in the effective electron density during the measurement phase, we consider the constant value given above a good approximation.

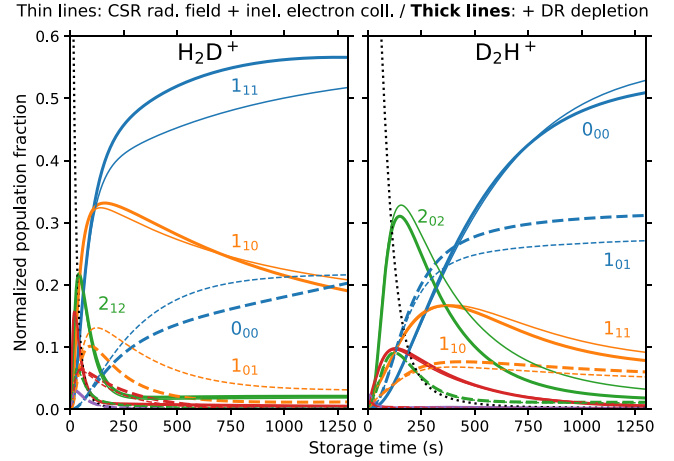


FIG. 7. Calculated evolution of the relative populations of rotational states of H_2D^+ and D_2H^+ during storage. The thick lines depict a model that includes radiative transitions, inelastic electron collisions and state-selective depletion by DR. The thin lines represent the evolution without DR depletion. Ortho states are shown by solid lines, para states are shown by dashed lines. The color code for the individual levels is adapted from Fig. 2. The dotted black lines show the evolution of the sum of the populations in states with $J > 2$.

The convolution of the theoretical cross sections with the electron velocity profile resulted in merged-beams rate coefficients for inelastic collisions in the range of $10^{-7} \text{ cm}^3 \text{ s}^{-1}$ or below at typical cooling energies. Since the electron density in our experiment was comparatively low ($\leq 1 \times 10^5 \text{ cm}^{-3}$), and the 0.7 m overlap inside the electron target is only a small fraction of the 35 m circumference of the storage ring, one can estimate the effective rate for the strongest transitions through inelastic electron collisions to be on the order of 10^{-4} s^{-1} . Because neither H_2D^+ nor D_2H^+ possess metastable states, the radiative transitions among all higher-lying states are much faster, when compared to inelastic electron collisions. Consequently, radiative processes dominate the internal cooling at early times. However, the effect of inelastic electron collisions does influence the final-state relative populations by up to 5% for H_2D^+ and 10% for D_2H^+ .

Calculated thermal rate coefficients for inelastic electron collisions will be made available through the EMAA database [52].

C. Depletion of individual states by DR

Finally, to get the best estimate of the evolution of the individual states during our measurements, we also included depletion through the DR process (see Fig. 7). We used the calculated DR merged-beams rate coefficients from our updated calculations (Figs. 3 and 4) as loss processes for those specific rotational states.

While the inclusion of depletion by DR affects the final relative state populations for H_2D^+ by a few percentages, the effect is even smaller for D_2H^+ , mainly due to the low DR rate coefficients predicted by theory for the lowest rotational states of D_2H^+ . Although this final correction applied to the experimental results is based on theory, the smallness of the correction ensures that a quantitative comparison of experi-

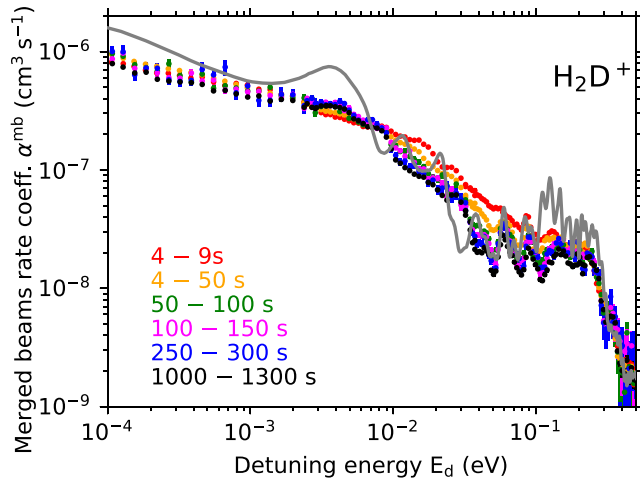


FIG. 8. Measured merged-beams DR rate coefficient of H_2D^+ for various storage time intervals inside the CSR. The error bars represent only the one-sigma uncertainty derived from counting statistics. We estimate an additional uncertainty of 20% for the absolute scale. The gray solid line represents the theoretical prediction for the longest storage time interval (1000–1300 s).

mental and theoretical results remains valid. It is important to note that DR depletion is the only process in the model that can shift the canonical ortho to para ratio for both ions, as radiation and inelastic collisions do not change the nuclear spin.

In summary, the master equation approach predicts population distributions after 1300 s that are confined to the three lowest rotational states for H_2D^+ , and the five lowest states for D_2H^+ . One has to keep in mind that both ions feature two different nuclear spin configurations and one cannot expect radiative cooling to occur between these manifolds. Therefore, for H_2D^+ the 1_{10} ortho state is in essence the only excited state left; and with a lifetime of 8197 s, it requires a prohibitively long time to decay spontaneously for our experiments. For D_2H^+ , the model predicts that five states carry significant populations after 1000 s of storage. For both ions the ortho states carry more population than the para states, which is consistent with their larger statistical weights of 9:3 for H_2D^+ and 12:6 for D_2H^+ (see Table I).

V. RESULTS

Figures 8 and 9 depict the measured merged-beams DR rate coefficients for H_2D^+ and D_2H^+ , respectively, as a function of storage time. Each storage time period shown in Figs. 8 and 9 was preceded by a cooling phase, during which the electron cooler was set to nominal cooling energy at an electron density of $1.1 \times 10^5 \text{ cm}^{-3}$, with a duty cycle of 50%. This duty cycle was implemented to limit beam depletion by the DR process, and it was realized by switching the electron beam on and off with 50-ms time periods. The effective electron density for the cooling phase is thus $0.55 \times 10^5 \text{ cm}^{-3}$. During the given measurement intervals the electron beam energy was rapidly scanned between a variable measurement value, a fixed reference energy for normalization and the nominal beam cooling energy, with millisecond-long time

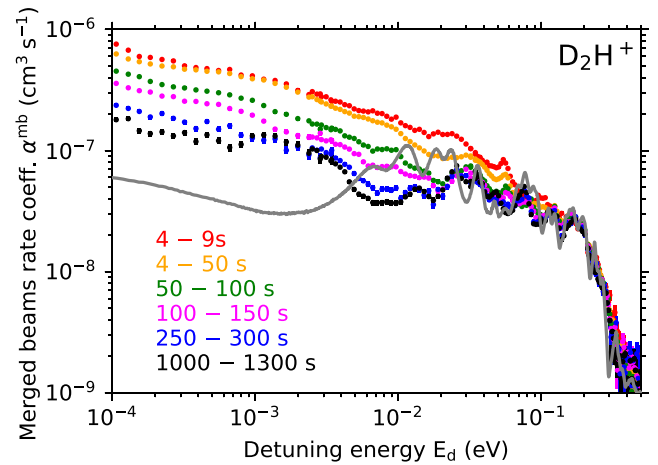


FIG. 9. Measured merged-beams DR rate coefficient of D_2H^+ for various storage time intervals inside the CSR. The error bars represent only the one-sigma uncertainty derived from counting statistics. We estimate an additional uncertainty of 20% for the absolute scale. The gray solid line represents the theoretical prediction for the longest storage time interval (1000–1300 s).

steps. The exact measurement timing scheme was adapted throughout the campaign, depending on the duration of the measurement phase as well as the duration of the overall injection cycle.

Comparing the temporal evolution of the DR rate coefficient for both ions reveals clear differences. For H_2D^+ , the low-energy-rate coefficient (at $E_d < 10^{-2} \text{ eV}$) does not change much as the storage time increases, while for D_2H^+ a steady reduction of the low-energy rate coefficient with storage time is visible. It is interesting to compare this behavior with the calculated state-selective DR rate coefficients and the predicted rotational state evolution. For each ion the calculations indicate that the energetically lowest state features a slow DR rate coefficient (see Figs. 3 and 4). However, for D_2H^+ the absolute scale of the rate coefficient for the 0_{00} state is almost an order of magnitude lower than for H_2D^+ at the lowest detuning energies. Furthermore, also the lowest D_2H^+ para state 1_{01} and the first excited states in each nuclear spin manifold (ortho- 1_{11} and para- 1_{10}) have calculated rate coefficients that drop below $10^{-8} \text{ cm}^3 \text{ s}^{-1}$ at the lowest collision energies. For H_2D^+ , on the other hand, only the energetically lowest para- 0_{00} state features a low calculated rate coefficient, and this state never accumulates more than 20% of the total population (see Fig. 7). Therefore, the observed trends in the time evolution of the DR rate coefficients of the experimental data at detuning energies below 10^{-2} eV are compatible with the calculated state-specific DR rate coefficients for both ions.

Also shown in the figures are the theoretical DR rate coefficients for the longest storage time interval of 1000–1300 s (gray lines). The theoretical curves represent the calculated state-selective merged-beams DR rate coefficients that were weighted with their relative populations for the given storage time interval, as derived from the model of the rotational state evolution. The overall shape and scale of the theoretical DR rate coefficients compare favorably with the experimental data. There is a clear discrepancy, however, between

experiment and theory for D_2H^+ at the lowest detuning energies. It is presently unclear whether this is caused by deficiencies in either theory or experiment. At the very lowest energies, the theoretical description becomes increasingly sensitive to the exact position of individual Rydberg resonances, which are difficult to predict with milli-electronvolt accuracy. The experimental data, on the other hand, start to be impacted by the experimental resolution, as the transverse temperature of the electron beam is estimated to be on the order of 2 meV.

Some of the discrepancy for the low-energy-rate coefficient of D_2H^+ at long storage times could be explained if the simulated evolution of the rotational states predicts a final population in the 0_{00} state that is too high. As this ground state has a very low calculated rate coefficient, the theoretical curve would be higher if other states were to be included with a higher fractional population. However, this effect cannot explain the discrepancy in its entirety. Additional theoretical and experimental studies are foreseen to shed light on this issue. It should also be noted that the log-log representation of the data overemphasizes the very lowest detuning energies.

At intermediate energies (10^{-2} eV $< E_d < 10^{-1}$ eV) the measured DR rate coefficients of both ions appear smooth at short storage times, but clear structures become visible at long storage times. These structures are caused by rotational resonances, which are present in all calculated state-specific rate coefficients (see Figs. 3 and 4); however, as hundreds of rotational states are populated at the earliest storage times, the structures are washed out by the superposition of many individual states. A more detailed compilation of the time evolution of the rate coefficients for both experiment and theory will be presented in Fig. 10.

To facilitate a clearer representation of the resonant structures, we plot the storage time-dependent *reduced* merged-beams rate coefficient $\sqrt{E_d} \alpha^{mb}$ for both ions in Fig. 10. This particular scaling of the DR rate coefficient has been applied previously [14,23], as it effectively removes the intrinsic $1/\sqrt{E}$ -threshold dependence of the rotational resonances, such that the presentation of the rate coefficient on a linear scale becomes informative.

In the linear representation the rate coefficients for both ions show the same trend as in the log-log plots, but the structures at long storage times are now more clearly defined. In particular, the time evolution of the D_2H^+ rate coefficient reveals interesting dynamics, as some peaks vanish during storage, while others appear.

For all storage time intervals that start at times >50 s we also plot our theoretical merged-beams rate coefficients. These curves result from the calculated individual rate coefficients weighted with the respective individual state populations (given in the insets), as predicted by the simulation of the rotational state populations (Fig. 7). Note that for the shorter storage times significant fractions of the total population may be occupying higher-lying rotational states (with $J > 1$ for H_2D^+ and $J > 2$ for D_2H^+). The theoretical curves were not corrected for this higher-lying population, i.e., at shorter storage times only a fraction of the total population is accounted for by the theoretical rate coefficients. For the shortest storage time interval (4–9 s) we did not plot any theoretical data, as the population in the low-lying rotational

states, for which calculated rate coefficients are available, was $<10\%$ in both cases.

Overall, the detailed experiment-theory comparison that the reduced rate coefficient affords appears more favorable for the case of D_2H^+ . As discussed previously [23], the resonance structures for storage times >1000 s are well represented by theory at detuning energies $E_d > 30$ meV. For H_2D^+ , on the other hand, all structures appear significantly sharper in the theoretical curves across the entire detuning energy range. The origin of this difference in the behavior for both isotopologs is presently unclear, as the theoretical approach and the experimental techniques that were used are identical.

It is possible that the rotational cooling model is less accurate for H_2D^+ , and more states are populated in the experiment than the model predicts. This would lead to a smearing of the resonances in the experimental data. However, we presently see no reason why the model should work better for D_2H^+ than for H_2D^+ .

It is therefore currently not possible to determine conclusively what causes the difference between theory and experiment in the sharpness and definition of the individual resonances. The present calculations employ an energy-independent scattering matrix, which limits the accuracy of the theoretical model at lower energies. For the future, there are plans to apply the energy-dependent frame transformation approach—as demonstrated for diatomic ions in Ref. [53]—to the various triatomic hydrogen isotopologs. We hope this will help to shed light on the issue.

To facilitate the inclusion of the rate coefficients into chemical models of interstellar cloud chemistry or plasma applications, we have converted the experimental H_2D^+ merged-beams DR rate coefficient of cold H_2D^+ (storage time >1000 s) into a thermal gas kinetic rate coefficient (the D_2H^+ kinetic temperature DR rate coefficient was already reported in the supporting material of Ref. [23]). The procedure is outlined in the Appendix and two different sets of fit parameters are provided.

VI. SUMMARY AND CONCLUSION

We have measured the DR of the deuterated hydrogen ions H_2D^+ and D_2H^+ with unprecedented definition of the internal states, employing the CSR electron cooler and very long storage times. We simulated the internal state evolution for both ions using state-of-the-art theoretical data for radiative transitions, inelastic electron collisions, and (as a small correction) state-selective depletion by the DR process itself. Our comprehensive master equation model predicts that after 1000 s of storage inside the CSR only a handful of identifiable rotational states remain populated.

The evolution of the DR rate coefficient for different storage time intervals shows clear differences for the two isotopologs. While the low-energy rate coefficient changes only slightly for H_2D^+ , the rate coefficient of D_2H^+ decreases steadily with storage time at low detuning energies. This observed trend is compatible with the theoretical prediction of very low rate coefficients for the lowest rotational states of D_2H^+ .

Comparison of the DR rate coefficients for the cold ions across all detuning energies with the theoretical calculations

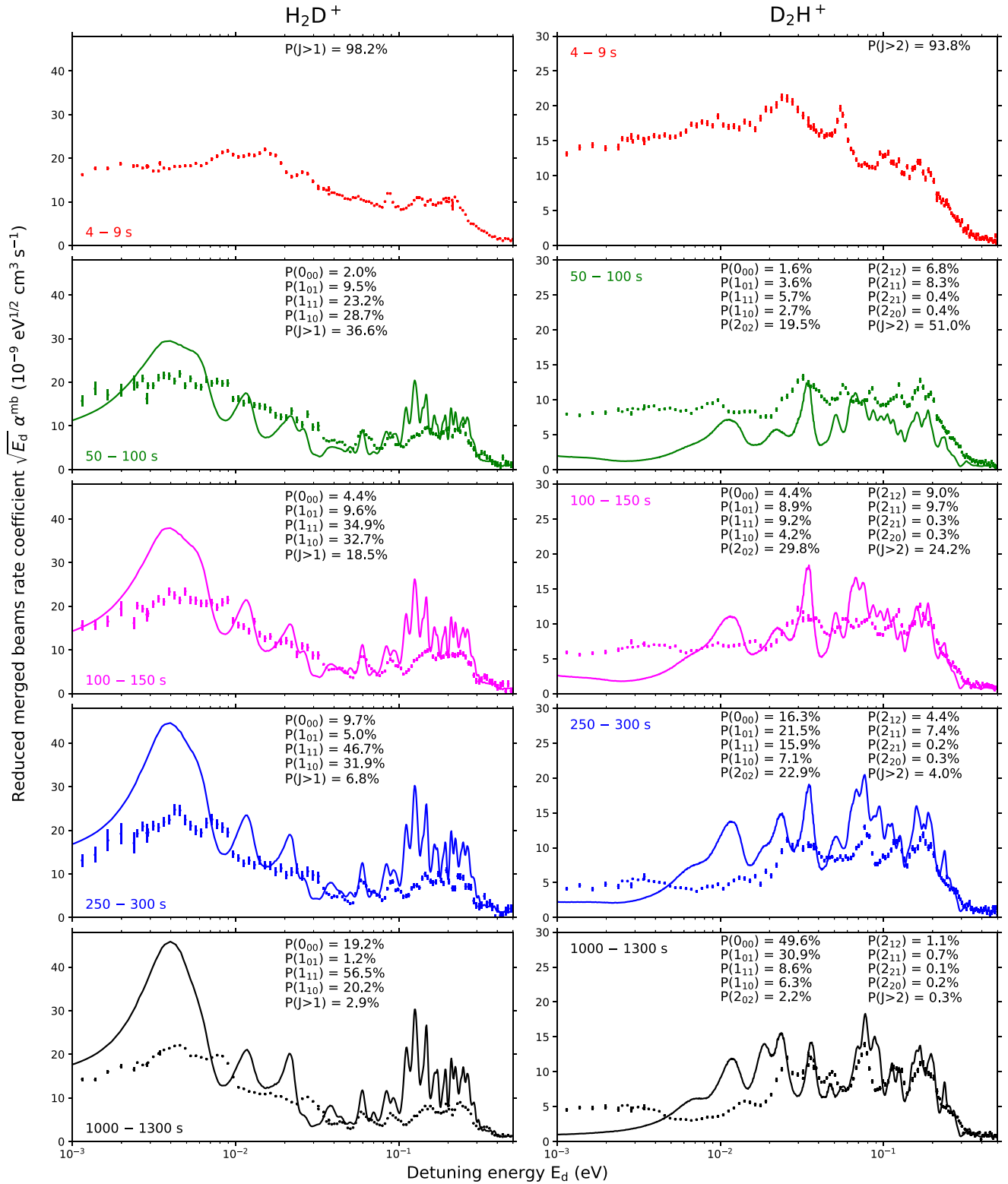


FIG. 10. Experimental reduced merged-beams DR rate coefficient $\sqrt{E_d} \alpha^{\text{mb}}$ for H_2D^+ (left-hand panel) and D_2H^+ (right-hand panel) for different storage time intervals. The simulated population of the 4 (9) lowest rotational states for H_2D^+ (D_2H^+) is given in the insets together with the sum of the populations in all states with $J > 1$ ($J > 2$). For storage time intervals that start at least 50 s after the ion injection, the weighted theoretical DR rate coefficients are also plotted (full lines). The individual state contributions were derived from the simulation of the internal state evolution. The missing contributions of higher-lying states ($J > 1$ for H_2D^+ and $J > 2$ for D_2H^+) have not been included in the plots of the theoretical rate coefficients.

show good agreement overall; however, distinct discrepancies remain between experiment and theory for D_2H^+ at detuning energies below 20 meV.

To focus on the resonant structures arising from the indirect mechanism, we plotted the reduced DR rate coefficient $\sqrt{E_d} \alpha^{mb}$ as a function of storage time in the CSR. The presentation reveals very interesting dynamics, in particular for the D_2H^+ ion, where certain features in the rate coefficient appear and vanish during storage. We are presently not yet able to assign individual resonances to initial rotational states, but further studies are foreseen.

In order to continue to improve the DR experiments at the CSR, we are currently developing techniques to diagnose and change the populations of individual rotational states with laser light for the H_3^+ molecular ion. Once these techniques are functional, we will be able to manipulate individual state populations in a well-defined procedure and compare the measured impact on the DR rate coefficient to the corresponding theoretical predictions.

Overall, we anticipate that our experiments and theoretical calculations for the most fundamental triatomic molecules pave the way for a better understanding of the complex DR process of polyatomic molecular ions.

ACKNOWLEDGMENTS

This work was supported by the Max Planck Society. We thank Z. Mašín for providing details on his ASYMTOP code. C.H.G. is supported by the U.S. Department of Energy, Office of Science, Basic Energy Sciences, under Award No. DE-SC0010545. The work performed at UCL was supported by the European Research Council (ERC) under the European Union's Horizon 2020 research and innovation programme through Advanced Grant No. 883830. A.K., D.P., and D.W.S. were supported, in part, by the National Science Foundation Astronomy and Astrophysics Grants Program under Grant No. AST-1907188 and the NASA Astrophysics Research and Analysis Program under Grants No. 80NSSC19K0696 and No. 80NSSC24K0206. L.W.I. and S.S. are grateful for financial support by the Deutsche Forschungsgemeinschaft via Project No. 431145392.

DATA AVAILABILITY

The data that support the findings of this article are not publicly available upon publication because it is not technically feasible and/or the cost of preparing, depositing, and hosting the data would be prohibitive within the terms of this research project. The data are available from the authors upon reasonable request.

APPENDIX: THERMAL GAS KINETIC DR RATE COEFFICIENT FOR H_2D^+

We have converted our experimental merged-beams DR rate coefficient $\alpha^{mb}(E_d)$ for rotationally cold H_2D^+ (storage time > 1000 s) into a gas kinetic $\alpha^k(T_k)$ thermal rate coefficient in order to enable the inclusion of the new data in astrochemical models or plasma simulations. We already pro-

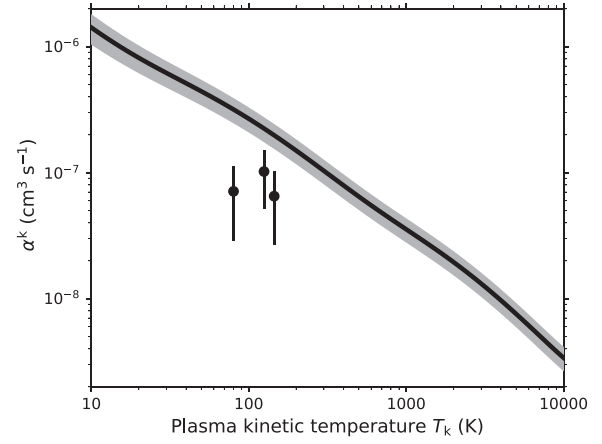


FIG. 11. Thermal rate coefficient for H_2D^+ as a function of the kinetic gas temperature. The DR rate coefficient (black lines) was derived from the cold experimental merged-beams rate coefficients (measured after 1000 s of storage) by the procedure outlined in the text. The gray error bands signify one-sigma uncertainties that have been propagated through the numerical procedure, where the dominating factors for the uncertainty of the absolute scale are the determination of the electron density and the number of ions stored in the ring. Results from afterglow studies [54] and their uncertainties are indicated by separate points.

vided the gas kinetic DR rate coefficient for cold D_2H^+ in a separate publication [23].

We apply a two-step procedure which has been described and employed in previous studies [20–23]. In the following, T_k denotes the kinetic temperature of the gas. First, we convert the experimental rate coefficient into a cross section $\sigma(E)$ as a function of the collision energy E . To this end we make use of the known merged-beams energy distribution $f_{mb}(E; E_d)$, which is a function of the detuning energy E_d . We use an iterative procedure (described in detail in Ref. [37]), using the relation

$$\alpha^{mb}(E_d) = \int_0^\infty \sigma(E) \sqrt{\frac{2E}{m_e}} f_{mb}(E; E_d) dE. \quad (A1)$$

We start by creating a discrete generic cross-section histogram and varying it until the application of Eq. (A1) reproduces the experimental rate coefficient. Once the cross section has been extracted, it can be convolved with a Maxwell-Boltzmann distribution for various kinetic temperatures T_k , using

$$\alpha^k(T_k) = \int_0^\infty \sigma(E) \sqrt{\frac{2E}{m_e}} \sqrt{\frac{4E}{\pi (k_B T_k)^3}} e^{-E/k_B T_k} dE. \quad (A2)$$

Figure 11 shows the gas kinetic DR rate coefficient for H_2D^+ as a function of the temperature. The total uncertainties of the experiment have been propagated through the two-step procedure; they are plotted in the figure as gray error bands. Also shown are the results of stationary afterglow studies at three different temperatures [54]. The afterglow experiments yielded lower rate coefficients. The reason for the discrepancy is presently unclear; however, afterglow studies are carried out at elevated pressure, which may lead to ternary collisions possibly affecting the measured rate coefficient [55].

TABLE II. Fit parameters for the kinetic temperature rate coefficient of H_2D^+ with their lower and upper uncertainty bounds, based on Eq. (A3) as the fit function.

	Value	Lower bound	Upper bound
A	1.47×10^{-07}	1.18×10^{-07}	6.81×10^{-08}
n	0.719	0.696	0.983
c_1	-4.20×10^{-05}	-2.88×10^{-05}	9.98×10^{-05}
c_2	-2.00×10^{-04}	-1.61×10^{-04}	-1.90×10^{-04}
c_3	-6.52×10^{-04}	-5.47×10^{-04}	1.95×10^{-04}
c_4	-1.12×10^{-03}	-1.03×10^{-03}	3.67×10^{-04}
c_5	-5.15×10^{-03}	-4.54×10^{-03}	1.57×10^{-03}
c_6	-1.61×10^{-02}	-1.46×10^{-02}	-8.02×10^{-04}
T_1	15.5	14.7	50.8
T_2	235	230	113
T_3	594	581	295
T_4	1513	1498	960
T_5	5144	5053	2366
T_6	15 315	15 257	12 717

Furthermore, the population of the individual rotational states may differ between our experiments and the afterglow studies, as in the latter case the ions' internal temperature should also reflect the kinetic temperature, while we expect the internal population for our data to be dominated by the three lowest rotational states, as predicted by the simulation for storage times > 1000 s (Fig. 7).

We present two analytical representations of the rate coefficient along with their associated one-sigma uncertainty ranges. The first model is a continuously differentiable function optimized to capture resonant DR features [37], such as peaks and dips. It is expressed as

$$\alpha^k(T_k)[\text{cm}^3 \text{s}^{-1}] = A \left(\frac{300}{T_k[\text{K}]} \right)^n + T_k[\text{K}]^{-1.5} \times \sum_{r=1}^8 c_r \exp\left(-\frac{T_r}{T_k[\text{K}]}\right), \quad (\text{A3})$$

where A , n , c_r , and T_r are fit parameters, the values of which are given in Table II. The relative deviation of the fit does not exceed 2.4%.

The second representation of the thermal rates utilizes Arrhenius-Kooij (AK) functions, commonly employed in astrochemistry, combustion chemistry, and related chemical model databases. However, the application of a single func-

TABLE III. Fit parameters for the H_2D^+ kinetic temperature rate coefficient and their relative uncertainty obtained using Eqs. (A4) and (A5) as the fit functions.

	Temperature range (K)		
	10–100	100–3000	3000–10 000
A_i	1.39×10^{-07}	1.01×10^{-07}	1.52×10^{-07}
β_i	-0.610	-0.873	-1.092
γ_i	-2.423	-5.637	-284.1
$F_{0,i}$	1.247	1.236	1.289
g_i	1.067	2.467	16.46

tion alone is insufficient to accurately model the kinetic rate coefficient across the entire temperature range. To that end, in line with the approach in Ref. [21], we use a set of piecewise-joined AK fit functions over selected temperature intervals

$$\alpha^k(T_k)[\text{cm}^3 \text{s}^{-1}] = A_i \left(\frac{T_k[\text{K}]}{300} \right)^{\beta_i} e^{-\frac{\gamma_i}{T_k[\text{K}]}} \quad (\text{A4})$$

where A_i , β_i , and γ_i are the fit parameters for various temperatures, listed in Table III.

The relative deviation of the fit to the data does not exceed 3.5%. In line with KIDA conventions [56] we provide the uncertainty of α^k by means of the log-normal factor $F = \exp(\Delta\alpha^k/\alpha^k)$. The value of $F(T_k)$ is determined by averaging the upper and lower one-sigma error bands. The subsequent fit is carried out over the same temperature intervals that were used for the AK functions, using the following fit function:

$$F(T_k) = F_{0,i} \exp\left(g_i \left(\frac{1}{T_k[\text{K}]} - \frac{1}{300} \right)\right), \quad (\text{A5})$$

where $F_{0,i}$ and g_i denote the fit parameters provided in Table III.

In addition, we have imposed the following conditions for parameters $F_{0,i}$ and A_i :

$$A_i = A_0 \prod_{j=1}^i \left(\frac{T_j}{300} \right)^{\beta_{j-1} - \beta_j} e^{\frac{\gamma_j - \gamma_{j-1}}{T_j}}, \quad (\text{A6})$$

and

$$F_{0,i} = F_{0,0} \exp\left(\frac{g_i - g_0}{300}\right) \prod_{j=1}^i \exp\left(\frac{g_{j-1} - g_j}{T_j}\right). \quad (\text{A7})$$

Unlike equations (A4) and (A5) alone, these additional relations ensure continuous behavior of the fit functions at the boundaries of the temperature intervals.

[1] The Cologne Database for Molecular Spectroscopy—Molecules in Space, <https://cdms.astro.uni-koeln.de/classic/molecules>
[2] E. Herbst and W. Klemperer, *Astrophys. J.* **185**, 505 (1973).
[3] W. D. Watson, *Astrophys. J.* **183**, L17 (1973).
[4] T. Oka, *Chem. Rev.* **113**, 8738 (2013).
[5] S. Miller, J. Tennyson, T. R. Geballe, and T. Stallard, *Rev. Mod. Phys.* **92**, 035003 (2020).
[6] G. Pineau Des Forêts and E. Roueff, *Phil. Trans. R. Soc. A* **358**, 2549 (2000).

[7] B. J. McCall, A. J. Huneycutt, R. J. Saykally, T. R. Geballe, N. Djuric, G. H. Dunn, J. Semaniak, O. Novotny, A. Al-Khalili, A. Ehlerding, F. Hellberg, S. Kalhori, A. Neau, R. Thomas, F. Österdahl, and M. Larsson, *Nature (Lond.)* **422**, 500 (2003).
[8] M. Larsson, B. McCall, and A. Orel, *Chem. Phys. Lett.* **462**, 145 (2008).
[9] M. Larsson and A. E. Orel, *Dissociative Recombination of Molecular Ions*, Cambridge Molecular Science (Cambridge University Press, Cambridge, UK, 2008).

- [10] R. Johnsen and S. L. Guberman, *Adv. At. Mol. Opt. Phys.* **59**, 75 (2010).
- [11] B. J. McCall, A. J. Huneycutt, R. J. Saykally, N. Djuric, G. H. Dunn, J. Semaniak, O. Novotny, A. Al-Khalili, A. Ehlerding, F. Hellberg, S. Kalhori, A. Neau, R. D. Thomas, A. Paal, F. Österdahl, and M. Larsson, *Phys. Rev. A* **70**, 052716 (2004).
- [12] H. Kreckel, M. Motsch, J. Mikosch, J. Glosík, R. Plašil, S. Altevogt, V. Andrianarijaona, H. Buhr, J. Hoffmann, L. Lammich, M. Lestinsky, I. Nevo, S. Novotny, D. A. Orlov, H. B. Pedersen, F. Sprenger, A. S. Terekhov, J. Toker, R. Wester, D. Gerlich *et al.*, *Phys. Rev. Lett.* **95**, 263201 (2005).
- [13] H. Kreckel, O. Novotný, K. N. Crabtree, H. Buhr, A. Petrigiani, B. A. Tom, R. D. Thomas, M. H. Berg, D. Bing, M. Grieser, C. Krantz, M. Lestinsky, M. B. Mendes, C. Nordhorn, R. Repnow, J. Stützel, A. Wolf, and B. J. McCall, *Phys. Rev. A* **82**, 042715 (2010).
- [14] A. Petrigiani, S. Altevogt, M. H. Berg, D. Bing, M. Grieser, J. Hoffmann, B. Jordon-Thaden, C. Krantz, M. B. Mendes, O. Novotný, S. Novotny, D. A. Orlov, R. Repnow, T. Sorg, J. Stützel, A. Wolf, H. Buhr, H. Kreckel, V. Kokoouline, and C. H. Greene, *Phys. Rev. A* **83**, 032711 (2011).
- [15] H. Kreckel, A. Petrigiani, O. Novotný, K. Crabtree, H. Buhr, B. J. McCall, and A. Wolf, *Philos. Trans. R. Soc. A* **370**, 5088 (2012).
- [16] V. Kokoouline, C. H. Greene, and B. D. Esry, *Nature (Lond.)* **412**, 891 (2001).
- [17] V. Kokoouline and C. H. Greene, *Phys. Rev. Lett.* **90**, 133201 (2003).
- [18] S. F. dos Santos, V. Kokoouline, and C. H. Greene, *J. Chem. Phys.* **127**, 124309 (2007).
- [19] C. Jungen and S. T. Pratt, *Phys. Rev. Lett.* **102**, 023201 (2009).
- [20] O. Novotný, P. Wilhelm, D. Paul, Á. Kálosi, S. Saurabh, A. Becker, K. Blaum, S. George, J. Göck, M. Grieser, F. Grussie, R. von Hahn, C. Krantz, H. Kreckel, C. Meyer, P. M. Mishra, D. Muell, F. Nuesslein, D. A. Orlov, M. Rimmler *et al.*, *Science* **365**, 676 (2019).
- [21] D. Paul, M. Grieser, F. Grussie, R. von Hahn, L. W. Isberner, Á. Kálosi, C. Krantz, H. Kreckel, D. Müll, D. A. Neufeld, D. W. Savin, S. Schippers, P. Wilhelm, A. Wolf, M. G. Wolfire, and O. Novotný, *Astrophys. J.* **939**, 122 (2022).
- [22] Á. Kálosi, L. Gamer, M. Grieser, R. von Hahn, L. W. Isberner, J. I. Jäger, H. Kreckel, D. A. Neufeld, D. Paul, D. W. Savin *et al.*, *Astrophys. J. Lett.* **955**, L26 (2023).
- [23] A. Znotins, A. Faure, C. H. Greene, M. Grieser, F. Grussie, L. W. Isberner, Á. Kálosi, V. Kokoouline, D. Müll, D. Paul, M. Pezzella, D. W. Savin, S. Schippers, J. Tennyson, A. Wolf, O. Novotný, and H. Kreckel, *Nat. Commun.* **16**, 7738 (2025).
- [24] A. Znotins, F. Grussie, A. Wolf, X. Urbain, and H. Kreckel, *J. Mol. Spectrosc.* **378**, 111476 (2021).
- [25] N. Indriolo, T. R. Geballe, T. Oka, and B. J. McCall, *Astrophys. J.* **671**, 1736 (2007).
- [26] T. Oka, *Philos. Trans. R. Soc. A* **377**, 20180402 (2019).
- [27] M. Goto, T. Usuda, T. Nagata, T. R. Geballe, B. J. McCall, N. Indriolo, H. Suto, T. Henning, C. P. Morong, and T. Oka, *Astrophys. J.* **688**, 306 (2008).
- [28] F. Le Petit, M. Ruaud, E. Bron, B. Godard, E. Roueff, D. Languignon, and J. Le Bourlot, *Astron. Astrophys.* **585**, A105 (2016).
- [29] T. Oka, T. R. Geballe, M. Goto, T. Usuda, Benjamin, J. McCall, and N. Indriolo, *Astrophys. J.* **883**, 54 (2019).
- [30] S. Brünken, O. Sipilä, E. T. Chambers, J. Harju, P. Caselli, O. Asvany, C. E. Honingh, T. Kamiński, K. M. Menten, J. Stutzki *et al.*, *Nature (Lond.)* **516**, 219 (2014).
- [31] L. Pagani, A. Belloche, and B. Parise, *Astron. Astrophys.* **691**, A88 (2024).
- [32] L. Pagani, C. Vastel, E. Hugo, V. Kokoouline, C. H. Greene, A. Bacmann, E. Bayet, C. Ceccarelli, R. Peng, and S. Schlemmer, *Astron. Astrophys.* **494**, 623 (2009).
- [33] R. von Hahn, A. Becker, F. Berg, K. Blaum, C. Breitenfeldt, H. Fadil, F. Fellenberger, M. Froese, S. George, J. Göck, M. Grieser, F. Grussie, E. A. Guerin, O. Heber, P. Herwig, J. Karthein, C. Krantz, H. Kreckel, M. Lange, F. Laux *et al.*, *Rev. Sci. Instrum.* **87**, 063115 (2016).
- [34] H. Poth, *Phys. Rep.* **196**, 135 (1990).
- [35] M. Grieser, V. C. Schmidt, K. Blaum, F. Grussie, R. von Hahn, Á. Kálosi, H. Kreckel, D. Müll, O. Novotný, F. Nuesslein, and A. Wolf, *Rev. Sci. Instrum.* **93**, 063302 (2022).
- [36] A. Shornikov, D. A. Orlov, C. Krantz, A. S. Jaroshevich, and A. Wolf, *Phys. Rev. ST Accel. Beams* **17**, 042802 (2014).
- [37] O. Novotný, A. Becker, H. Buhr, C. Domesle, W. Geppert, M. Grieser, C. Krantz, H. Kreckel, R. Repnow, D. Schwalm, K. Spruck, J. Stützel, B. Yang, A. Wolf, and D. W. Savin, *Astrophys. J.* **777**, 54 (2013).
- [38] H. H. Michels and R. H. Hobbs, *Astrophys. J.* **286**, L27 (1984).
- [39] A. E. Orel and K. C. Kulander, *Phys. Rev. Lett.* **71**, 4315 (1993).
- [40] I. F. Schneider, A. E. Orel, and A. Suzor-Weiner, *Phys. Rev. Lett.* **85**, 3785 (2000).
- [41] C. A. Bowesman, I. I. Mizus, N. F. Zobov, O. L. Polyansky, J. Sarka, B. Poirier, M. Pezzella, S. N. Yurchenko, and J. Tennyson, *Mon. Not. R. Astron. Soc.* **519**, 6333 (2023).
- [42] V. Kokoouline and C. H. Greene, *Phys. Rev. A* **72**, 022712 (2005).
- [43] V. Kokoouline and C. H. Greene, *Phys. Rev. A* **68**, 012703 (2003).
- [44] I. Mistrík, R. Reichle, U. Müller, H. Helm, M. Jungen, and J. A. Stephens, *Phys. Rev. A* **61**, 033410 (2000).
- [45] F. Merkt, K. Höveler, and J. Deiglmayr, *J. Phys. Chem. Lett.* **13**, 864 (2022).
- [46] H. Kreckel, S. Krohn, L. Lammich, M. Lange, J. Levin, M. Scheffel, D. Schwalm, J. Tennyson, Z. Vager, R. Wester, A. Wolf, and D. Zajfman, *Phys. Rev. A* **66**, 052509 (2002).
- [47] K. P. Bowen, P. M. Hillenbrand, J. Liévin, D. W. Savin, and X. Urbain, *J. Chem. Phys.* **154**, 084307 (2021).
- [48] T. Sochi and J. Tennyson, *Mon. Not. R. Astron. Soc.* **405**, 2345 (2010).
- [49] S. C. Foster, A. R. W. McKellar, and J. K. G. Watson, *J. Chem. Phys.* **85**, 664 (1986).
- [50] H. Kreckel, J. Tennyson, D. Schwalm, D. Zajfman, and A. Wolf, *New J. Phys.* **6**, 151 (2004).
- [51] C. Meyer, A. Becker, K. Blaum, C. Breitenfeldt, S. George, J. Göck, M. Grieser, F. Grussie, E. A. Guerin, R. von Hahn, P. Herwig, C. Krantz, H. Kreckel, J. Lion, S. Lohmann, P. M. Mishra, O. Novotný, A. P. O'Connor, R. Repnow, S. Saurabh *et al.*, *Phys. Rev. Lett.* **119**, 023202 (2017).
- [52] A. Faure, A. Bacmann, and R. Jacquot, *Astron. Astrophys.* **700**, A266 (2025).
- [53] D. Hvizdoš, R. Čurík, and C. H. Greene, *Phys. Rev. A* **111**, 012805 (2025).
- [54] R. Plašil, P. Dohnal, Á. Kálosi, Š. Roučka, R. Johnsen, and J. Glosík, *Plasma Sources Sci. Technol.* **26**, 035006 (2017).

- [55] J. Glosík, R. Plašil, I. Korolov, T. Kotřík, O. Novotný, P. Hlavenka, P. Dohnal, J. Varju, V. Kokoouline, and C. H. Greene, [Phys. Rev. A **79**, 052707 \(2009\)](#).
- [56] V. Wakelam, E. Herbst, J.-C. Loison, I. W. M. Smith, V. Chandrasekaran, B. Pavone, N. G. Adams, M.-C. Bacchus-Montabonel, A. Bergeat, K. Béroff, V. M. Bierbaum, M. Chabot, A. Dalgarno, E. F. van Dishoeck, A. Faure, W. D. Geppert, D. Gerlich, D. Galli, E. Hébrard, F. Hersant *et al.*, [Astrophys. J. Suppl. Ser. **199**, 21 \(2012\)](#).